REVIEW ARTICLE | FOCUS
PUBLISHED ONLINE: 6 OCTOBER 2014 | DOI: 10.1038/NNANO.2014.215
nature nanotechnology

Photodetectors based on graphene, other two-dimensional materials and hybrid systems

F. H. L. Koppens[1*], T. Mueller[2], Ph. Avouris[3], A. C. Ferrari[4], M. S. Vitiello[5] and M. Polini[5,6]

Graphene and other two-dimensional materials, such as transition metal dichalcogenides, have rapidly established themselves as intriguing building blocks for optoelectronic applications, with a strong focus on various photodetection platforms. The versatility of these material systems enables their application in areas including ultrafast and ultrasensitive detection of light in the ultraviolet, visible, infrared and terahertz frequency ranges. These detectors can be integrated with other photonic components based on the same material, as well as with silicon photonic and electronic technologies. Here, we provide an overview and evaluation of state-of-the-art photodetectors based on graphene, other two-dimensional materials, and hybrid systems based on the combination of different two-dimensional crystals or of two-dimensional crystals and other (nano)materials, such as plasmonic nanoparticles, semiconductors, quantum dots, or their integration with (silicon) waveguides.

The conversion of light into electrical signals is at the heart of a multitude of technologies that affect our daily lives. Applications, including video imaging, optical communications, biomedical imaging, security, night-vision, gas sensing and motion detection have reached a high level of maturity due to the development of high-performance materials and large-scale production and integration technologies. Although the scale and diversity of application areas are growing, the need for a photodetection platform with higher performance in terms of speed, efficiency or wavelength range, as well as flexibility, transparency and complementary metal–oxide–semiconductor (CMOS) integrability, is becoming more eminent.

Graphene is an appealing material for photonics and optoelectronics because it offers several advantages compared with other materials[1–5]. A variety of prototype optoelectronic devices have already been demonstrated, such as transparent electrodes in displays[6] and photovoltaic modules[7,8], optical modulators[9], plasmonic devices[10] and ultrafast lasers[3]. Among these, significant effort has been devoted to developing photodetectors, based on a number of distinct characteristics of graphene and related materials (GRMs). First, graphene is gapless. This enables charge carrier generation by light absorption over a very wide energy spectrum, unmatched by any other material. This includes the ultraviolet, visible, short-wave infrared (SWIR), near-infrared (NIR), mid-infrared (MIR), far-infrared (FIR) and terahertz (THz) spectral regimes. Furthermore, graphene exhibits ultrafast carrier dynamics[11,12], wavelength-independent absorption[13–15], tunable optical properties via electrostatic doping[16,17], low dissipation rates and high mobility, and the ability to confine electromagnetic energy to unprecedented small volumes[4,5]. The high carrier mobility enables ultrafast conversion of photons or plasmons to electrical currents or voltages[18,19].

Many of the characteristics and unique capabilities of photodetection systems based on graphene have been studied over the past few years, and several applications have been addressed. Some of these have already reached a level of competitiveness with existing technologies that may spark interest for commercialization. Importantly, graphene is compatible with the highly mature silicon-based platform for electronics and photonics[20–22], making it a strong contender for low-cost and large-scale integration into optoelectronic networks and multipixel CMOS read-out circuits.

Graphene is just one of a large number of possible two-dimensional (2D) crystals that are only now beginning to be investigated[23,24]. There are hundreds of layered materials that retain their stability down to monolayers, and whose properties are complementary to those of graphene. Transition metal oxides (TMOs) and transition metal dichalcogenides (TMDs) have a layered structure[25]. Atoms within each layer are held together by covalent bonds, while different layers are mainly held together by van der Waals interactions[25]. Compared with classical direct-bandgap semiconductors, TMDs can offer additional advantages in the context of optoelectronics because of their transparency, mechanical flexibility and easy processing. Moreover, the ability to tune the bandgap by varying the number of layers (*N*) allows the detection of light at different wavelengths. These properties complement those of graphene in many ways: graphene is useful for broadband, ultrafast technologies, whereas semiconducting TMDs are advantageous for applications requiring strong light absorption and electroluminescence. A promising approach is to combine these properties and create multifunctional, high-performance materials consisting of graphene and other 2D crystal heterogeneous stacks and hybrid devices. Graphene layers can be employed as work-function tunable electrodes, while TMDs are utilized as photoactive material, displaying strong light–matter interaction and photon absorption.

In this Review, we discuss the current state-of-the-art of photodetectors based on GRMs and hybrid systems realized by the combination of different 2D crystals or of 2D crystals and other (nano) materials, such as plasmonic nanoparticles, quantum dots (QDs), or by the integration of GRMs with silicon waveguides. First, the terminology and basic physical mechanisms of photodetection are discussed, then the experimental realizations of various kinds of photodetector, including techniques to enhance sensitivities and light absorption. We conclude with a critical discussion on the level of maturity and performance of current state-of-the-art GRM photodetection platforms in comparison with existing technologies.

Physical mechanisms enabling photodetection

The key principle on which photodetection and other optoelectronic applications rely is the conversion of absorbed photons into an electrical signal. Several different mechanisms by which this can

---

[1]ICFO-Institut de Ciencies Fotoniques, Mediterranean Technology Park, 08860, Castelldefels, Barcelona, Spain, [2]Vienna University of Technology, Institute of Photonics, Gußhausstraße 27-29, 1040 Vienna, Austria, [3]IBM Thomas J. Watson Research Center, Yorktown Heights, New York 10598, USA, [4]Cambridge Graphene Centre, 9 JJ Thomson Avenue, Cambridge CB3 0FA, UK, [5]NEST, Istituto Nanoscienze-CNR and Scuola Normale Superiore, I-56126 Pisa, Italy, [6]Istituto Italiano di Tecnologia, Graphene Labs, Via Morego 30, I-16163 Genova, Italy. *e-mail: frank.koppens@icfo.es

be accomplished in graphene have been reported. These include the photovoltaic effect, the photo-thermoelectric effect, the bolometric effect, the photogating effect and the plasma-wave-assisted mechanism. In the following, we describe these mechanisms, when each of them may become dominant and their manifestations in GRM-based photodetectors.

Note that the relevant terminology, units and key figures of merits for photodetectors (such as the concepts of photocurrent, speed, internal and external quantum efficiencies, responsivity, detectivity, noise-equivalent power and photoconductive gain) are summarized in Box 1.

Photovoltaic effect. Photovoltaic (PV) photocurrent generation is based on the separation of photogenerated electron–hole (e–h) pairs by built-in electric fields at junctions between positively (p-type) and negatively (n-type) doped regions of graphene or between differently doped sections[26–28] (Fig. 1b,d). The same effect can be achieved by applying a source–drain bias voltage (V_{bias}), producing an external electric field. But this is generally avoided in the case of graphene, as it is a semimetal and therefore it generates a large dark current. The built-in field can be introduced either by local chemical doping[29], electrostatically by the use of (split) gates[26,30], or by taking advantage of the work-function difference between graphene and a contacting metal[26–28,31]. In the case of split gates, the doping can be tuned to be p or n, depending on the applied gate voltages, whereas in the case of graphene–metal junctions the doping in the contacted area is fixed. This is typically p-type for metals with a work function higher than that of intrinsic graphene (4.45 eV), whereas the graphene channel can be p or n. The photocurrent direction depends only on the direction of the electric field, not on the overall doping level. Thus, it switches sign when going from p–n to n–p, or from p–p$^+$ to p$^+$–p, where p$^+$ means stronger p-type doping compared with p.

We note that electron–electron (e–e) scattering[32–34] can lead to the conversion of one high-energy e–h pair into multiple e–h pairs of lower energy[12,33,35]. This process, also denoted as carrier multiplication, can potentially enhance the overall photodetection efficiency.

Photo-thermoelectric effect. Hot-carrier-assisted transport can play an important role in graphene[30,36–39] (Fig. 1a–d). Because of strong e–e interactions[40], a photoexcited e–h pair will lead to ultrafast (~10–50 fs) heating of the carriers in graphene[41–44]. Because the optical phonon energy in graphene is large[45,46] (~200 meV), hot carriers created by the radiation field can remain at a temperature T_{e} (and thus energy $k_{\mathrm{B}}T_{\mathrm{e}}$, with k_{B} the Boltzmann constant) higher than that of the lattice for many picoseconds. Final equilibration of the hot electrons and the lattice occurs via the slower scattering between charge carriers and acoustic phonons[47,48]. These processes take place on a nanosecond timescale[47], although they experience a substantial speed-up attributed to disorder-assisted collisions[49–51].

The photogenerated hot electrons can produce a photovoltage, V_{PTE}, by the photo-thermoelectric (PTE) effect (Seebeck effect): $V_{\mathrm{PTE}} = (S_1 - S_2)\Delta T_{\mathrm{e}}$, where $S_{1,2}$ (in V K^{-1}) is the thermoelectric power (Seebeck coefficient) in the two graphene regions with different dopings, and ΔT_{e} is the electron temperature difference between the regions. More generically, V_{PTE} can be calculated by integrating the local electric field generated by an optically induced temperature gradient, ∇T_{e}, together with a spatially varying Seebeck coefficient: $V_{\mathrm{PTE}} = \int S \cdot \nabla T_{\mathrm{e}}\,\mathrm{d}x$. The PTE effect can dominate in graphene p–n junctions[30,37] or in suspended graphene[52]. Because hot electrons, rather than lattice heating, generate the electronic response under these conditions, PTE graphene detectors can achieve high bandwidths, as in the case of PV detectors. The thermoelectric power S (also called thermopower) is related to the electrical conductivity σ by the Mott formula[53]:

$$S = -\frac{\pi^2 k_{\mathrm{B}}^2 T_{\mathrm{e}}}{3q}\frac{1}{\sigma}\frac{\partial\sigma}{\partial\varepsilon} \qquad (1)$$

where q is the electron charge, and the derivative of the electrical conductivity σ with respect to energy ε must be evaluated at the Fermi energy, that is, at $\varepsilon = \varepsilon_{\mathrm{F}} = \hbar v_{\mathrm{F}} k_{\mathrm{F}}$, with $\hbar$ the reduced Planck constant, v_{F} the Fermi velocity (which in graphene[54] is ~10^6 m s^{-1}) and k_{F} the Fermi wavevector. Note that, because equation (1) was derived by utilizing the Sommerfeld expansion[53], it is valid only for $k_{\mathrm{B}}T << \varepsilon_{\mathrm{F}}$. For this condition, S can be calculated from the transport characteristics of the device, that is, from the dependence of conductance on gate voltage. A typical curve with the dependence of S on carrier density (n) is shown in Fig. 1b.

Box 1 | Terminology and key figures of merit in photodetectors.

Light impinging on a device, with a photon energy E_{ph} and power P_{in}, corresponds to an incoming photon flux $\phi_{\mathrm{in}} = P_{\mathrm{in}}/E_{\mathrm{ph}}$, and an absorbed photon flux $\phi_{\mathrm{abs}} = \phi_{\mathrm{in}}A_{\mathrm{abs}}$, with A_{abs} the absorbed fraction. The external quantum efficiency, EQE, is equal to the number of electron–hole (e–h) pairs per second collected to produce the photocurrent I_{ph}, divided by the number of incident photons per second: $\mathrm{EQE} = (I_{\mathrm{ph}}/q)/\phi_{\mathrm{in}}$, where q is the electron charge. The internal quantum efficiency (IQE) is calculated in a similar way except that in this case the absorbed photon flux is considered: $\mathrm{IQE} = (I_{\mathrm{ph}}/q)/\phi_{\mathrm{abs}}$. The responsivity of a photodetector is the photocurrent I_{ph} divided by the incident power: $R_{\mathrm{ph}} = I_{\mathrm{ph}}/P_{\mathrm{in}}$, or, if the photoinduced voltage, V_{ph}, is measured, $R_{\mathrm{v}} = V_{\mathrm{ph}}/P_{\mathrm{in}}$. For example, in a detector with 100% EQE, $R_{\mathrm{ph}} = 1$ A W^{-1} for $E_{\mathrm{ph}} = 1$ eV. The noise equivalent power (NEP) is the signal power where the signal-to-noise ratio is unity, usually expressed in units of W Hz$^{-0.5}$. Another typical figure of merit used to characterize the performance of a detector is the specific detectivity D^*, which is given by $D^* = (A{\cdot}\mathrm{BW})^{0.5}/\mathrm{NEP}$. D^* is measured in cm Hz$^{1/2}$ W^{-1}, this unit was named after R. C. Jones, whereby 1 cm Hz$^{1/2}$ W^{-1} = 1 Jones, in recognition of his work on sensitivity of radiation sensors. Here, A is the area of the photosensitive region, and BW is the frequency bandwidth of the detector.

For sensitized photoconductors the external quantum efficiency is defined as $\mathrm{QE} = \eta_{\mathrm{trans}}\,\eta_{\mathrm{abs}}$, where η_{trans} is the charge transfer efficiency and η_{abs} is the light absorption efficiency. A second important parameter is the lifetime, τ_{tr}, of the charge residing in the particles, as the light-induced change in carrier density Δn scales linearly with it: $\Delta n = \tau_{\mathrm{tr}} \times \mathrm{QE} \times \phi_{\mathrm{in}}$. Photoconductive detectors are often benchmarked by their photoconductive gain, $G_{\mathrm{ph}} = (I_{\mathrm{ph}}/q)/(\phi_{\mathrm{in}}\mathrm{QE})$, that is, the number of detected charge carriers per single incident photon. This can be quantified by the ratio of the lifetime of the trapped carriers over the drift transit time, τ_{transit}, of the SLG charge carriers from source to drain: $G_{\mathrm{ph}} = \tau_{\mathrm{tr}}/\tau_{\mathrm{transit}}$. τ_{transit} is governed by the applied field, thus it is shorter for higher bias and mobility: $\tau_{\mathrm{transit}} = L^2/(\mu V_{\mathrm{bias}})$, with L the source–drain separation distance.

Bolometric effect. The bolometric effect is associated with the change in the transport conductance produced by heating associated with the incident photons (Fig. 1d). A bolometer measures the power of electromagnetic radiation by absorbing the incident radiation (dP) and reading out the resulting temperature increase dT. Bolometers

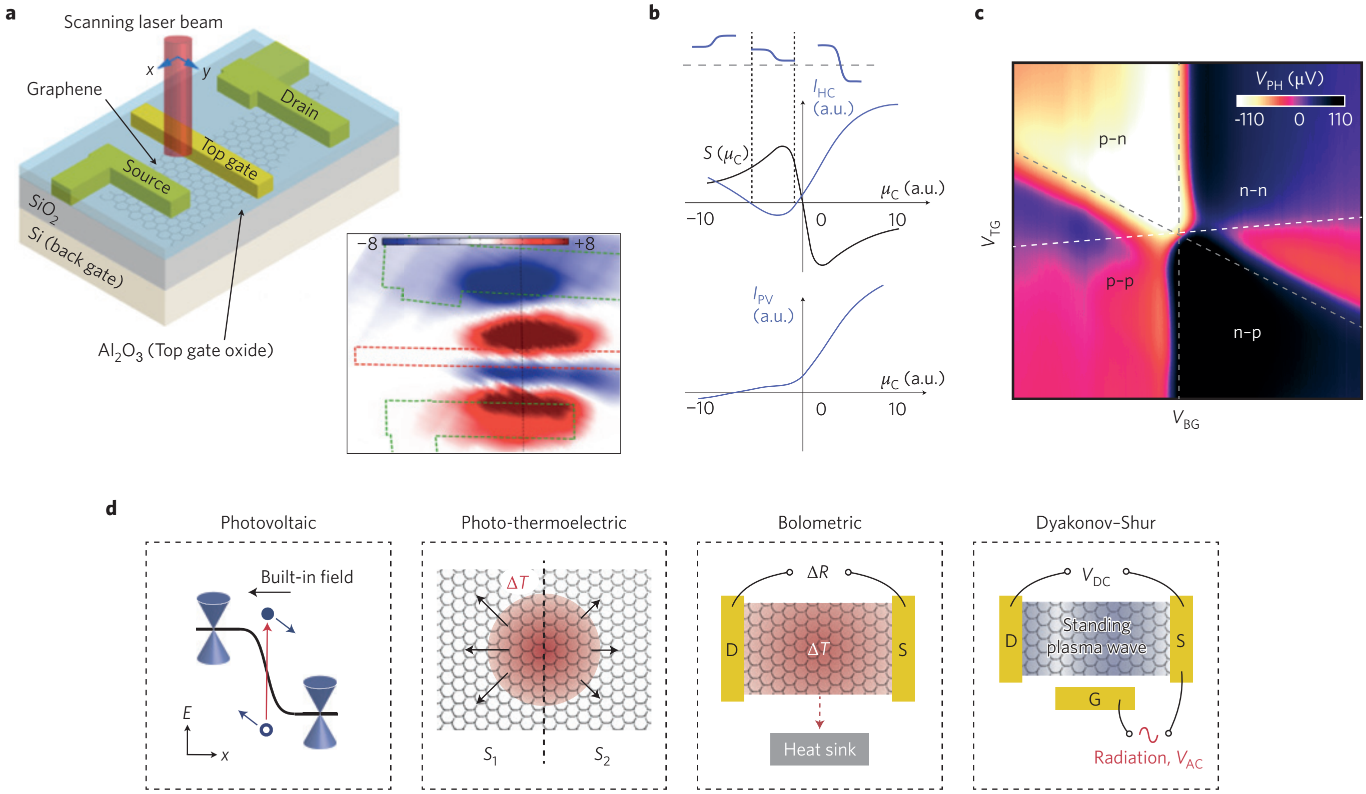

Figure 1 | Photodetection mechanisms. **a**, Top: Schematic of the double-gated device used to evaluate the PTE effect in ref. 30. By applying appropriate biases to the top (V_{TG}) and back (V_{BG}) gates, two differently doped graphene regions are created. Bottom: Scanning photocurrent of the device[30]. Dashed outlines indicate the contacts (green) and top gate (red). **b**, Calculation of the photocurrent from hot carriers (HC) and photovoltaic (PV) effects. The PV contribution changes sign when the electrical field changes sign, while the HC contribution changes sign twice. The chemical potential μ_C relative to the Dirac point (grey dashed line) is also plotted in the top graph. **c**, Photovoltage as a function of V_{BG} and V_{TG}. A sixfold change of polarity is observed. Grey dashed lines show high resistance as obtained from transport measurements. **d**, Schematic representation of the four photocurrent generation mechanisms discussed in the main text. First panel: electron–hole (solid and open circle) separation by an internal electric field. Second and third panels: red shaded area indicates elevated electron temperature with ΔT the temperature gradient and ΔR the resistance across the channel; S_1 and S_2, Seebeck coefficient in graphene areas with different doping. Third and fourth panels: S and D indicate source and drain, and G the gate; V_{DC}, photogenerated d.c. voltage; V_{AC}, a.c. voltage applied to the gate. Figures reproduced with permission from: **a**, ref. 30, © 2011 American Chemical Society; **b**, ref. 38, © 2011 American Chemical Society; **c**, ref. 37, © 2011 The American Association for the Advancement of Science.

are mainly made of semiconductor[55] or superconductor absorptive materials[56] and are widely used in the submillimetre (THz) wavelength range, where they are among the most sensitive detectors. The key parameters of a bolometer are the thermal resistance $R_h = dT/dP$, which ultimately defines its sensitivity, and the heat capacity C_h, which determines its response time $\tau = R_hC_h$ (ref. 56). Graphene has small volume for a given area and low density of states, which results in low C_h, thus a fast device response. The cooling of electrons by acoustic phonons is inefficient, owing to the small Fermi surface, and cooling by optical phonons requires high T_e ($k_BT_e > 0.2$ eV). Thus R_h is relatively high, giving rise to high bolometric sensitivity.

As this photodetection mechanism is based on a light-induced change in conductance, instead of direct photocurrent generation, it requires an externally applied bias and can operate on homogeneous graphene, without the need to introduce a p–n junction. The conductance change induced by the incident light can be due to two mechanisms: (1) a change in carrier mobility due to the associated temperature change; or (2) a change in the number of carriers contributing to the current. We note that (2) coincides with the PV effect, with the electric field generated by the external bias.

Photogating effect. The photogating effect is based on light-induced modification of the GRM carrier density Δn and therefore its conductance $\Delta\sigma = \Delta nq\mu$, where μ is the mobility. We can distinguish two cases. In the first, e–h pair generation takes place in the GRM, and subsequently one of the two carrier types (electrons or holes) is trapped (for example, in charge traps or in nearby molecules of nanoparticles). In the second, e–h pair generation takes place in nanoparticles, molecules or charge traps in the vicinity of the GRM. Subsequently, one type of carrier transfers to the GRM (in some cases driven by an internal field) and the other resides in the particles, molecules or traps, where they gate the GRM sheet, while the charges in the GRM are recirculated between source and drain[57]. We note the fundamental difference to the bolometric effect, which is based on the change in μ due to heating, is that the photogating effect is based on a light-induced change in n.

The photoconductive gain, G_{ph} (see Box 1 for definition) can be strongly enhanced by using a high-mobility conductor (such as graphene) and by a long τ_{tr} (see Box 1 for definition). At the same time, a long τ_{tr} reduces the operation speed. Therefore these detectors can be used for lower temporal bandwidth, such as video imaging applications. Photoconductive detectors may exhibit a high dark current, so a proper assessment of the detector performance is not just provided by the responsivity, but rather by measuring the noise-equivalent-power (NEP) or specific detectivity D^* (see Box 1 for definitions).

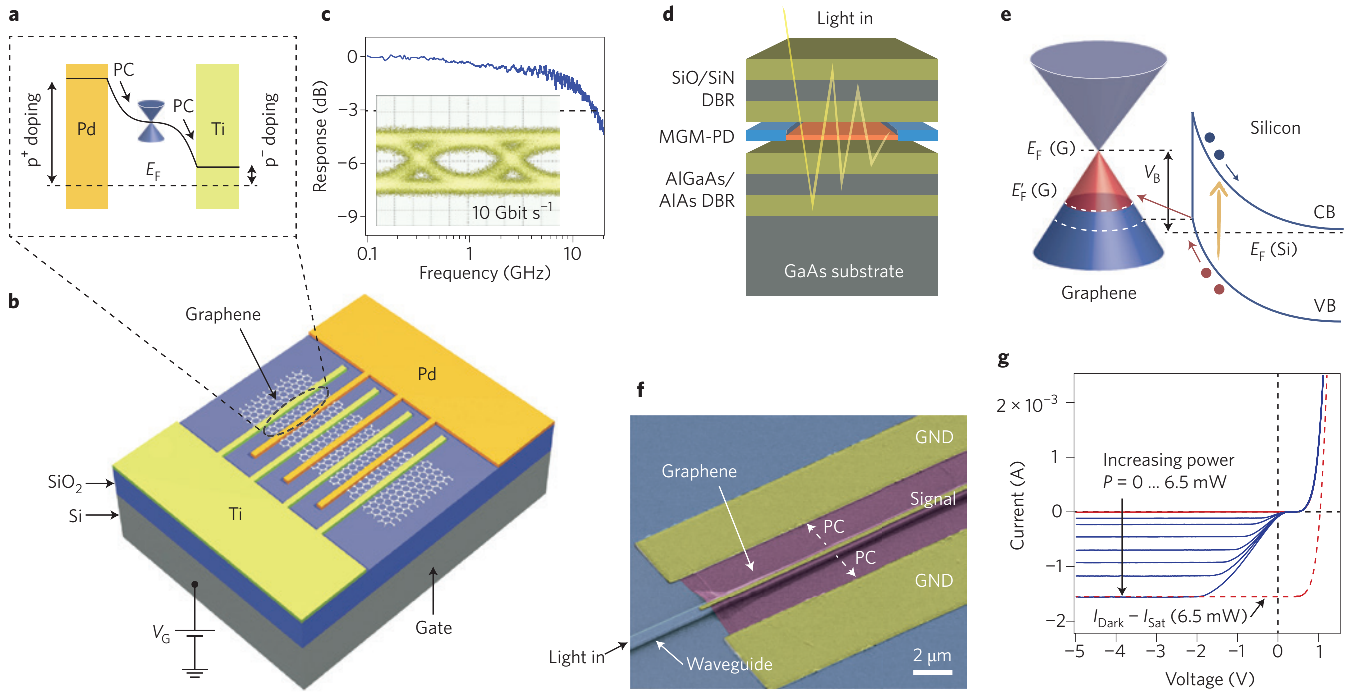

Figure 2 | Metal–graphene–metal and graphene–semiconductor heterojunction photodetectors. a, Band profile. The arrows indicate the electron flow and the Dirac cone indicates the charge neutrality point. PC, photocurrent; E_F, Fermi level. **b**, Three-dimensional schematic. **c**, High-frequency response of a metal–graphene–metal photodetector (MGM-PD) with asymmetric contacts. Inset: Eye diagram. **d**, Schematic layout of a microcavity-integrated photodetector. DBR, distributed Bragg mirror. **e**, Band profile (VB and CB, valence and conduction bands of silicon). **f**, Scanning electron microscope image of a waveguide-integrated device. GND, ground. **g**, I–V characteristics of a graphene–silicon heterojunction photodetector without (solid red line) and with (solid blue lines) illumination (with increments ~1 mW). The conventional photodiode behaviour (P = 6.5 mW) is shown as a red dashed line. The red portion of the Dirac cone in **e** denotes the holes injected from silicon. Figures reproduced with permission from: **a–c**, ref. 19, 2010 Nature Publishing Group; **f**, ref. 21, 2013 Nature Publishing Group; **e**,**g**, ref. 90, © 2013 American Chemical Society.

Plasma-wave-assisted mechanism. Dyakonov and Shur[58,59] proposed a photodetection scheme whereby a finite d.c. voltage is generated in a field-effect transistor (FET) in response to an oscillating radiation field (Fig. 1d). This is based on the fact that a FET hosting a 2D electron gas can act as a cavity for plasma waves (collective density oscillations)[60]. When these plasma waves are weakly damped (that is, when a plasma wave launched at the source can reach the drain in a time shorter than the momentum relaxation time)the detection of radiation exploits constructive interference of the plasma waves in the cavity, which results in a resonantly enhanced response. This is the so-called resonant regime of plasma-wave photodetection[59], and can give rise to a signal that is 5–20 times stronger than the broadband non-resonant signal. Broadband detection occurs when plasma waves are overdamped: that is, when plasma waves launched at the source decay before reaching the drain[59].

Dyakonov and Shur showed[59] that the photovoltage response of a 2D electron system in a FET, that is, the electric potential difference between drain and source, contains a d.c. component even if the incoming field is a.c., and thus provides rectification of the signal. This is particularly useful for the detection of THz radiation. Rectification occurs because of the nonlinear response of the 2D electron gas in the FET channel and is unrelated to extrinsic rectification mechanisms due to, for example, Schottky barriers at contacts or other circuital elements that respond in a non-ohmic manner. For the resonant regime, the d.c. photoresponse is characterized by peaks at odd multiples of the lowest plasma-wave frequency[59]. Resonant detection of THz radiation in graphene FETs was theoretically discussed in ref. 61, where the impact of hydrodynamic nonlinearities due to to the flow of the 2D electron gas in a graphene sheet was quantitatively addressed. Using the dispersion of plasma waves in graphene, the authors of ref. 61 concluded that the typical linear device size L required to operate in the THz spectral range varies between about 1 and 10 μm.

Room-temperature THz detectors based on antenna-coupled graphene FETs and exploiting the Dyakonov and Shur mechanism have been demonstrated[62,63]. In ref. 62 the plasma waves excited by THz radiation were overdamped, and thus the detectors did not operate in the resonant regime[61]. The dependence of the photovoltage on carrier density in the FET channel also displays PTE contributions[62,63].

Classes of photodetectors

We now discuss the main photodetector classes based on GRMs found in literature and address their relative merits and performances.

Metal–graphene–metal photodetectors. These were the first class of graphene-based photodetectors to be investigated[64–66]. In early reports[64–66], photocurrent was generated by local illumination of one of the metal/graphene interfaces of a back-gated graphene FET. The resulting current was attributed to the PV effect[64–66]. It was shown that the field arises from charge transfer from the respective contact metal to graphene[67,68], and can thus be adjusted by proper choice of the metal[65,69]. It can be further enhanced by doping via electrostatic gating[64–66]. Metal electrodes were also replaced by FeCl$_3$-intercalated graphene multilayers to realize an all-graphene-based photodetector[70].

In addition to the PV effect, the PTE effect can also contribute to photocurrent[36,39,71]. It was shown in refs 36,37,72 that the photoresponse near pn-junctions or interfaces of single-layer and bilayer

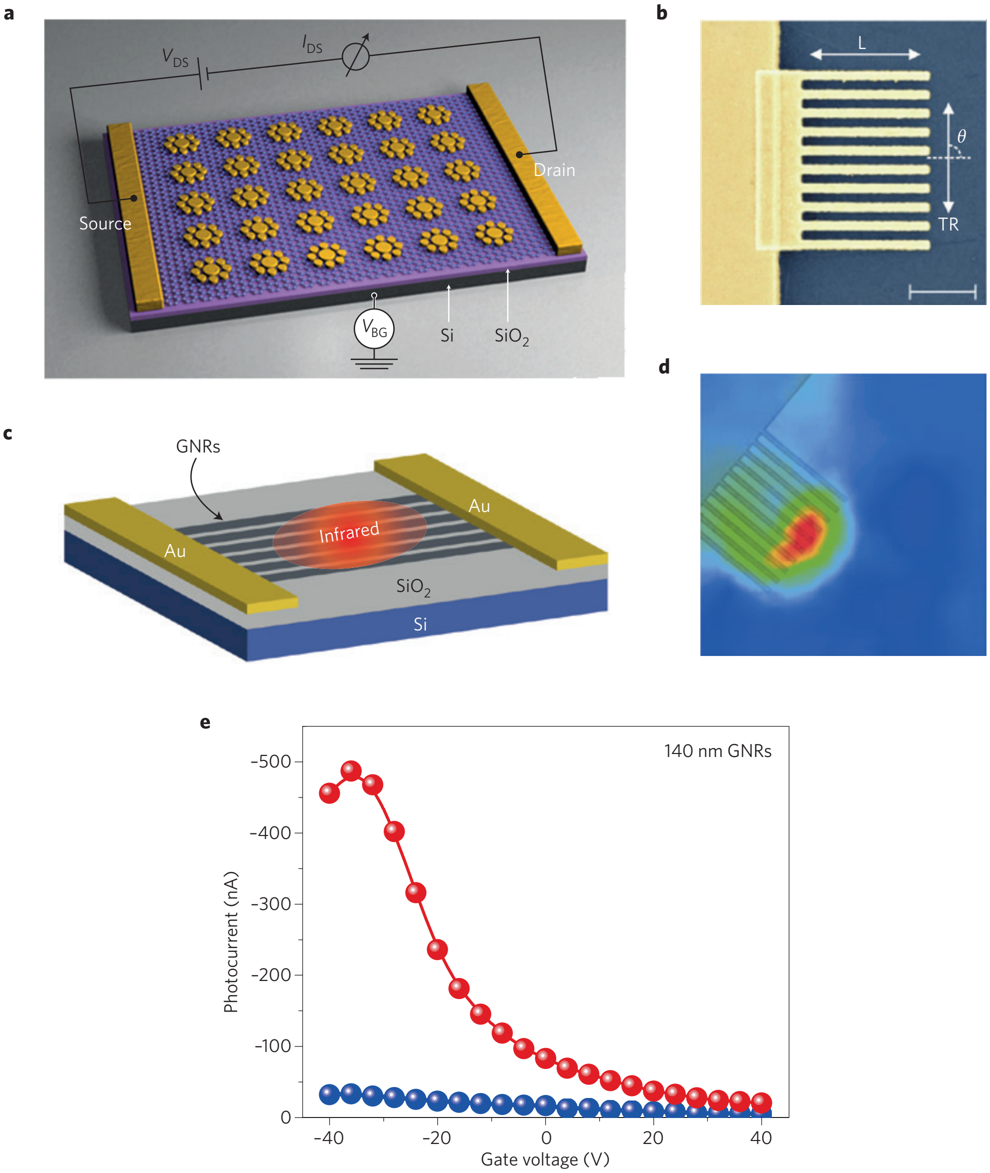

Figure 3 | Photodetection enhancement by metallic plasmonic nanostructures and intrinsic plasmons. a, Schematic of plasmonic antennas on SLG. **b**, Contact with a 'finger structure'. Longitudinal (L) and transverse (TR) incident light polarizations are indicated. Scale bar, 1 μm. **c**, Schematic illustration of a nanoribbon-array infrared photodetector. **d**, Photovoltage map of one of the nanostructured contacts, similar to the one shown in **b**. Colour scale runs from −4 μV (blue) to 12 μV (red). GNRs, graphene nanoribbons. **e**, Gate voltage dependence of the photocurrent of such a detector (ribbon width *W* = 140 nm) produced by a 10.6 μm light beam with a polarization perpendicular to the ribbons (red spheres), which allows plasmon excitation, and parallel to the ribbons (blue spheres), which does not couple to plasmons. Figures reproduced with permission from: **a**, ref. 113, © 2012 American Chemical Society; **b**,**d**, ref. 82, 2011 Nature Publishing Group; **c**,**e**, ref. 86, 2013 Nature Publishing Group.

graphene (SLG and BLG, respectively) was dominated by the PTE effect. In contrast to the PV current, the PTE current shows sign reversal in bipolar p–n junctions and also unipolar p^+p or nn^- junctions[37]. The sign changes because of the change in transconductance, $\partial\sigma/\partial\varepsilon$, on going from p- to n-type transport (Fig. 1b). Together with the sign reversal when switching the electric field direction, this leads to a sixfold sign change in the photocurrent[37] (Fig. 1c). Therefore, the sign of photocurrent due to the PV effect is opposite to that of the PTE current and can be used to differentiate between PV and PTE mechanisms (Fig. 1b). Wavelength and polarization measurements[73] of the photoresponse near the graphene–metal junction were used to quantify and control the relative contributions of PTE and PV effects, both adding to the overall photoresponse, with PV effects becoming more pronounced at longer wavelengths.

As the photocurrent generation occurs only in the submicrometre-wide[28] metal/graphene interface region, an interdigitated finger structure (Fig. 2b) was adopted to increase the effective photodetection area[19]. Applying a bias to break the mirror symmetry of the device is not practical, as graphene's semimetallic nature would give rise to a large dark current[19]. An asymmetric metallization scheme was thus employed (see band profile in Fig. 2a), which enabled zero-bias/dark current operation, and responsivities between 1.5 and 6.1 mA W^{-1} in the NIR. IQEs (see Box 1 for definition) of metal–graphene–metal photodetectors on Si/SiO_2 substrates are in the range[18] 6–16%, showing that there is room for improvement, as higher IQEs (~35%) were observed in suspended graphene[52].

The high carrier mobility and short carrier lifetime in graphene allow metal–graphene–metal photodetectors to operate at high data

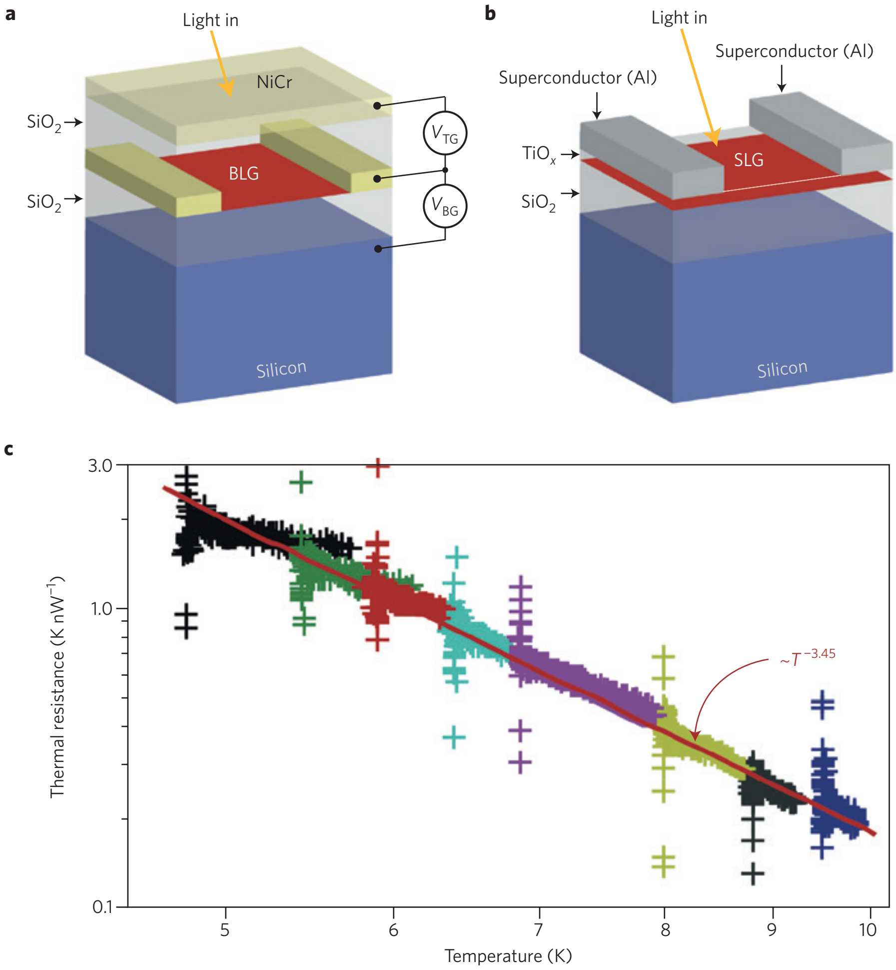

Figure 4 | Graphene-based bolometers. a, Device structure of a dual-gated bilayer graphene bolometer[94]. V_{TG}, top gate bias; V_{BG}, back gate bias. **b**, Device structure of a graphene–aluminium tunnel junction bolometer. **c**, Temperature dependence of heat resistance. The red line indicates the $T^{-3.45}$ temperature scaling. Figures reproduced with permission from: **a**,**c**, ref. 94, 2012 Nature Publishing Group; **b**, ref. 101, © 2012 American Institute of Physics.

rates. The device in Fig. 2b was deployed in an optical link and error-free recovery of a 10 Gbit s^{-1} data stream was achieved[19]. This is shown in Fig. 2c by the eye diagram, which is an overlay of different segments of a data stream and indicates the quality of signals in high-speed digital transmissions. In single metal–graphene junctions, no photoresponse degradation up to a modulation frequency of 40 GHz was observed[18], and an all-optical measurement[74] yielded an intrinsic bandwidth of 262 GHz. We note that not only PV but also PTE effects would be compatible with the experimentally observed high bandwidths, owing to the decoupling of electron and lattice temperatures[37,52].

Sensitivity enhancement by cavities, waveguides and plasmonics. SLG absorbs 2.3% of the incident light[14,15], which is remarkably high for an atomically thin material, but is very small in absolute terms. This is an appealing property for flexible and transparent optoelectronic devices. For certain applications, however, it is highly desirable to enhance the SLG absorption.

One approach to enhance absorption is based on integration into an optical microcavity[75,76] or planar photonic crystal cavities[77]. The cavity reported in ref. 75 (Fig. 2d) employed distributed Bragg reflectors, consisting of quarter-wavelength-thick layers of alternating materials, whereas in ref. 76 metallic mirrors were used. Incident light is trapped inside the planar cavity and passes multiple times through the SLG, giving rise to enhanced absorption. More than 60% light absorption and 21 mA W^{-1} responsivity were achieved[75]. Although the improved responsivity comes at the expense of spectral bandwidth, the design wavelength can be chosen, provided that a low-loss optical cavity can be realized in the desired wavelength range.

Another approach involves the coplanar integration of graphene with an optical waveguide[20–22]. This is illustrated in Fig. 2f (ref. 21): the optical mode in a silicon-on-insulator waveguide couples through its evanescent tail to a SLG deposited on top. An almost flat photoresponse across all-optical telecommunication windows (from O- to U-band) was demonstrated[21], well beyond the wavelength range of Ge detectors[78] (responsivities are limited on the long-wavelength side by the Ge bandgap). Bandwidths over 20 GHz and an open eye at 12 Gbit s^{-1} were obtained[20,21], indicating the potential for high-speed data transmission. The reported[20–22] responsivities, in the 0.05–0.13 A W^{-1} range, are on a par with state-of-the-art photodetectors made of GeSn (ref. 79) — as yet one of the most promising candidates for Si-compatible photodetector for long-wavelength (L and U) bands.

A third method to increase the photoresponse involves the use of the field enhancement resulting from the excitation of surface plasmons. Localized plasmons in metal nanostructures were first used in combination with graphene to achieve surface-enhanced Raman scattering[80], and to realize strong field enhancements in subnanometre gaps[81]. This was then applied to graphene-based

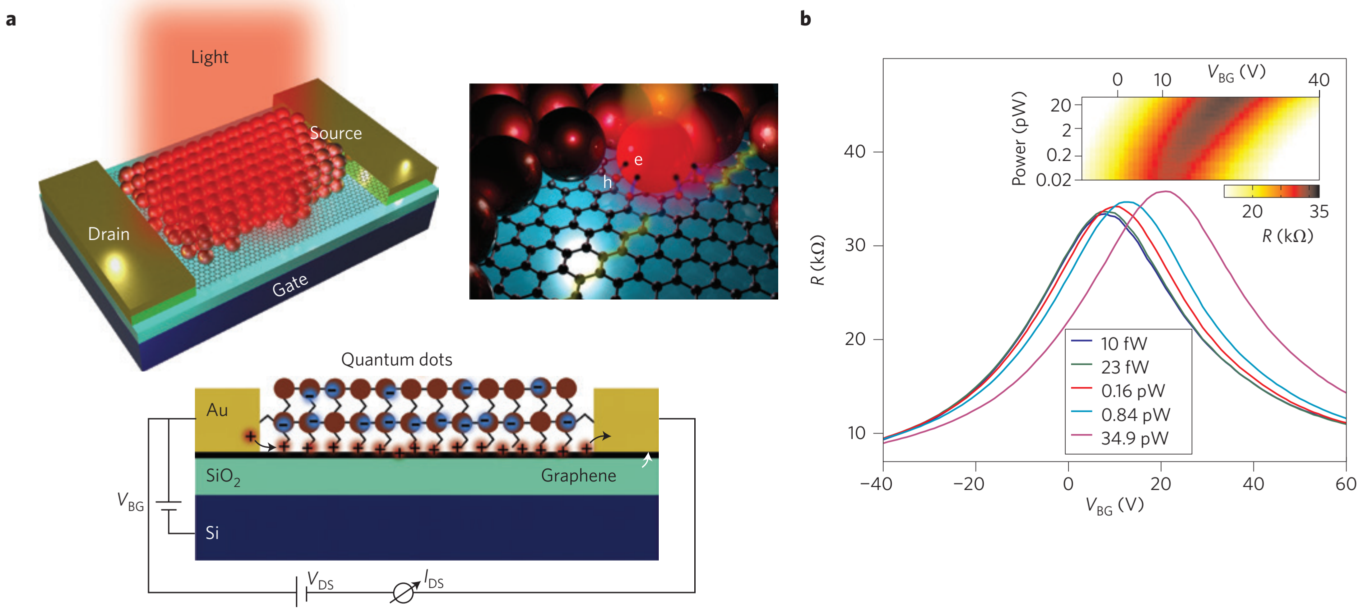

Figure 5 | Sensitized graphene photoconductive photodetectors. a, Photodetectors based on quantum dots (top left and bottom). The top right image shows the e–h separation in the quantum dot. **b**, Resistance as a function of back-gate voltage for the graphene–quantum dot structure for increasing illumination intensities. Increasing the illumination leads to a photogating effect that shifts the Dirac point to higher back-gate voltage, V_{BG}. This indicates hole photodoping of the graphene flake. Inset: Map of graphene resistance as a function of optical power. Figure reproduced with permission from ref. 105, 2012 Nature Publishing Group.

photodetectors, by placing the plasmonic nanostructures near the contacts[82] (Fig. 3a,b), which resulted in a significant improvement in performance (Fig. 3d). As an additional benefit, nanostructures with geometries resonant at desired wavelengths can be used for selective amplification, potentially allowing light filtering and detection, as well as polarization determination in a single device[83]. The frequency performance can be improved in comparison with traditional devices, as the plasmonic structures add only negligible contribution to the capacitance (fractions of femtofarads), but can significantly reduce the contact resistance. Another solution is to harvest light in a different region of the device and deliver it to the junction in graphene[73].

A fourth method for photodetector enhancement also exploits field enhancement by plasmons, but in this case the enhancement originates from the intrinsic collective charge oscillations of the 2D electron liquid inside graphene[5,10,84] (Fig. 3c,e). The ability to tune the plasmon wavelength and lifetime[4] by gating or doping could be crucial for many applications. The excellent carrier mobility in graphene and its 2D character lead to strong interaction enhancement between light and graphene, resulting in strong light absorption enhancements[85]. The ideal case would then be to use graphene itself as both photodetector and plasmonic enhancer. Indeed, graphene nanoribbon arrays on SiO$_2$ with different widths were demonstrated as room-temperature and tunable IR photodetectors[86]. As is shown in Fig. 3e, for a detector consisting of an array of 140 nm graphene nanoribbons, the enhancement is 1,500%[86].

Graphene–semiconductor heterojunction photodetectors. Planar junctions of graphene and group-IV elements[87–90], as well as compound semiconductors[91,92], can act as Schottky diodes. The electrical characteristics of these devices exhibit rectifying behaviour, with a barrier energy depending on the semiconductor material. For low dark current, semiconductor–graphene photodetectors are operated under reverse bias, and the corresponding band profile[90] is shown in Fig. 2e. Optical absorption takes place in the semiconductor, while SLG acts as an optically transparent charge carrier collector. As shown in Fig. 2g, semiconductor–graphene photodetectors deviate from a conventional (red dashed line) photodiode response: the photocurrent is suppressed for small bias voltages, V_B, as V_B controls E_F in graphene, hence controls the number of available states for photoexcited holes injected from the semiconductor under illumination[90]. This feature allowed voltage-tunable responsivity (up to 0.435 A W^{-1}) for brightness control and enabled operation over a large dynamic range of six orders of magnitude[90].

The spectral range was extended towards sub-bandgap wavelengths by electron excitation in graphene to energies above the Schottky barrier (internal photoemission)[93]. In Si–graphene junctions, IQE = 10% (for comparison, IQE ≈ 1% in regular Schottky diodes[55]) was obtained at telecommunication wavelengths[93], and a waveguide-integrated device[22] allowed MIR detection with 0.13 A W^{-1}, paving the way for high-performance, low-cost MIR photodetectors.

Graphene-based bolometers. By biasing SLG, bolometric responses were measured at room temperature[31,94]. In ref. 31 it was reported that two mechanisms result in bolometric photocurrents with opposite sign: the photoinduced excess carriers induce an enhancement of the conductance, whereas the temperature dependence of the mobility leads to a reduction of the conductance. By changing E_F, one can control which mechanism dominates[31]. Near the Dirac point, where the carrier density is lowest, PV effects dominate, whereas far away PTE effects dominate[31].

However, the weak temperature dependence of the electrical resistance in graphene[95] poses a major challenge for reading dT through electrical transport measurements. For this reason a small responsivity of 0.2 mA W^{-1} was measured for room-temperature graphene bolometric detectors[31]. To solve this problem, a dual-gated BLG device with an optically transparent top gate was used[94] (Fig. 4a) to open a bandgap at the Dirac point[96,97] and obtain T_e-dependent resistance[96]. The device was measured under MIR illumination (10.6 μm) using a four-terminal configuration, and the photoresponse was identified to be bolometric[94]. The

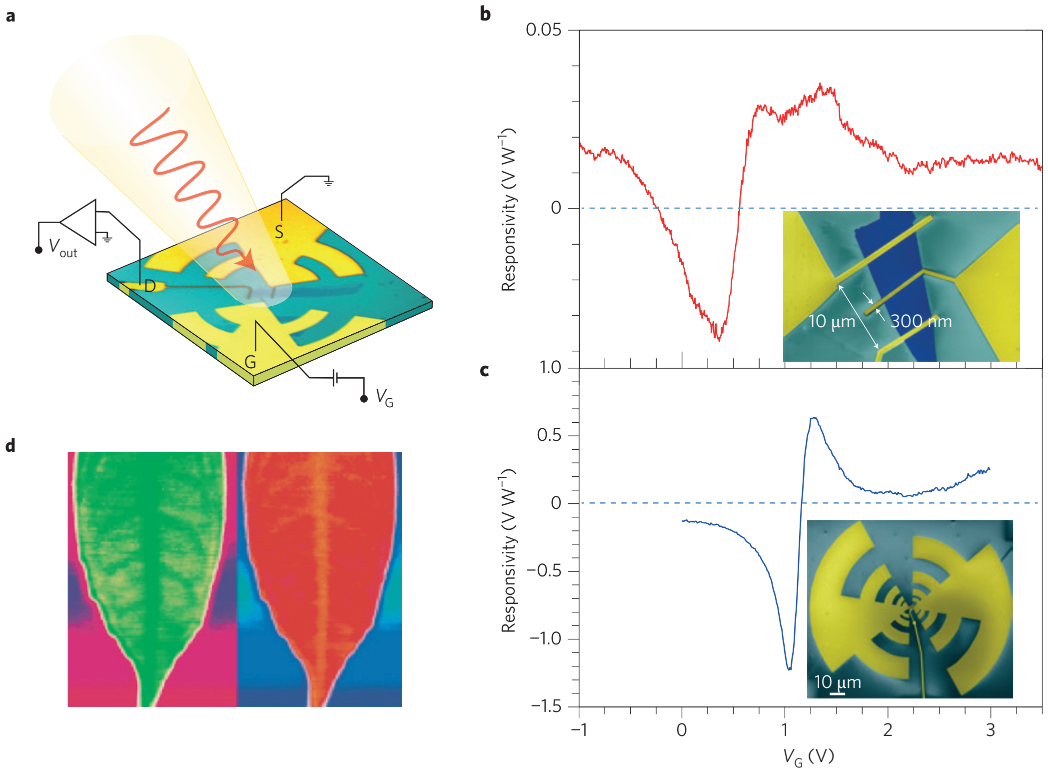

Figure 6 | Antenna-coupled graphene FET terahertz detector. a, The detector consists of a log-periodic circular-toothed antenna patterned between the source and gate of an SLG-FET. The drain is a metal line running to the bonding pad. **b**,**c**, Room-temperature responsivity as a function of the gate voltage, V_G, for detectors based on SLG-FET (**b**) and BLG-FET (**c**), as measured for the devices in ref. 62. Different background colours identify regions below and above the Dirac point. Insets: Scanning electron micrographs. **d**, Image (at 0.3 THz) of a leaf, which also reveals the leaf veins. Figure reproduced with permission from ref. 62, 2012 Nature Publishing Group.

thermal resistance, depicted in Fig. 4c, had a $T^{-3.45}$ dependence, which approximately agrees with the theoretically expected T^{-3} for (disorder-free) phonon cooling[98,99]. The detector exhibits excellent performance: NEP ≈ 33 fW Hz$^{-0.5}$ at T = 5 K (several times lower than commercial Si or superconducting bolometers) and an intrinsic bandwidth more than 1 GHz (3–5 orders of magnitude higher). Another approach for implementing a temperature-dependent graphene resistance is to drive the electronic system into the strong localization regime by adding disorder. This was achieved at low temperature by using defective graphene films[100].

Figure 4b shows a graphene–superconductor tunnel junction bolometer[101]. Although the device in ref. 101 was measured with radiofrequency waves, the concept can also be applied for optical detection. See ref. 102 for a recent review.

Hybrid phototransistors. Photon detection at very low intensities, even approaching the single-photon level, requires a gain mechanism that can provide multiple electrical carriers per single incident photon. This can be achieved by using appropriate sensitizing centres that absorb light efficiently, followed by transfer of either electrons or holes into the conductor (photogating effect)[57,103,104]. The result is a shift of the typical resistance versus gate-voltage curve, as shown in Fig. 5b. Graphene is an excellent candidate for room-temperature high-gain photodetection because of its high mobility (thus short carrier transit time). Also, being a 2D material, its conductance is very sensitive to electrostatic perturbation by photogenerated carriers close to the surface.

Examples of light-absorbing particles used to sensitize graphene are colloidal QDs made of PbS (refs 105,106; Fig. 5a), CdS (ref. 107) or ZnO (ref. 108). QDs can have strong light absorption and bandgap tunability, controllable by varying the size, and can cover the absorption range from ultraviolet to SWIR[109]. They can be processed in solution and deposited by spin-coating[110], contact printing, or inkjet techniques[111]. Furthermore, the ligands at the QD surface can be tailored, for optimization of charge transfer between the QDs themselves, and between the QDs and graphene. Hybrid sensitized graphene photoconductive photodetectors were realized using colloidal PbS or ZnO QDs[105,106,108] as light-absorbing media. Efficient light absorption and charge transfer was reported, with total QE ~25%. High gain, up to 10^8, was observed[105,106] for graphene decorated with PbS QDs[105], corresponding to R_{ph} ~10^7 A W^{-1} (at room temperature) for low light intensities ~10^{-14} W. Given the high QE (>25%), video-imaging speed ~30–60 Hz and low projected NEP ~10^{-17} W, this hybrid system is a promising platform for visible and SWIR applications.

Graphene covered with biomolecules[112] also revealed photogating effects for visible light, as did samples combined with metallic nanoantennas[113]. In particular, the latter offers a wide range of wavelength sensitivity obtained by tuning the plasmon resonance through the shape of the antenna, potentially covering the IR wavelength range as well.

Terahertz photodetectors. Owing to the low energy of the associated photons, THz radiation (0.1–10 THz, 30–300 µm) can penetrate commonly used dielectrics that are opaque to visible and MIR light. This enables the detection of substance-specific spectroscopic features with a submillimetre diffraction-limited lateral resolution[114]. Owing to its high carrier mobility, graphene is a very promising material for the development of room-temperature detectors operating across the FIR, with high room-temperature performance for

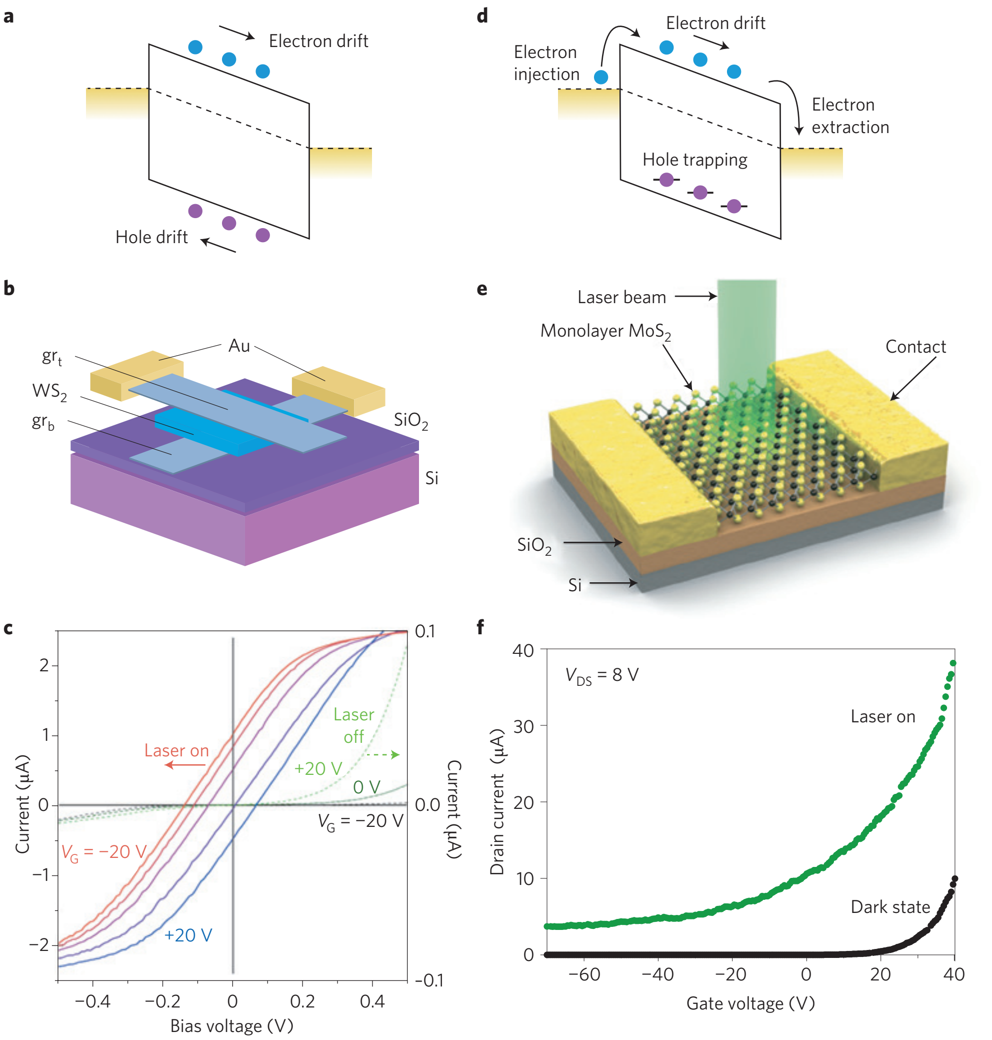

Figure 7 | Photodetection in a 1L-MoS$_2$ and in a SLG/WS$_2$/SLG heterostructure. a, Band diagram of a photodetector based on a 2D crystal, taking into consideration the bias voltage and small Schottky barriers at the contacts. **b**, A schematic of a SLG/WS$_2$/SLG heterostructure device, gr$_t$ and gr$_b$ are the top and bottom sheets of graphene, respectively. **c**, *I–V* curves for the SLG/WS$_2$/SLG heterostructure measured in ref. 147 under illumination (left axis) and in the dark (right axis). **d**, Band diagram of a photoconductive detector, taking into account hole trapping. **e**, Schematic view of a 1L-MoS$_2$ photodetector. **f**, Gating response of the MoS$_2$ photodetector of ref. 30 in dark and illuminated states. Figures reproduced with permission from: **b**,**c**, ref. 147, © 2013 The American Association for the Advancement of Science; **e**,**f**, ref. 130, 2013 Nature Publishing Group.

high spectral bandwidth covering the full THz range (0.1–10 THz). Graphene supports THz plasma waves that are potentially weakly damped (for length scales comparable to the source–drain distance) in high-mobility devices[115,116], allowing resonant detection in a FET[59,61]. A THz detection scheme based on a back-gated BLG-FET, with an interposed layer with high dielectric constant, in which the e–h pair generation would take place in the FET depleted section was suggested in ref. 117. The related variation in the source–drain electron current[117] was estimated to be proportional to the incident THz power. More recently, in ref. 118 it was suggested that graphene can be used for novel THz plasma-wave devices.

Room-temperature detection across the FIR was obtained in SLG and BLG plasma-wave FETs employing a top-gate antenna-coupled configuration (Fig. 6a) for the excitation of overdamped plasma-waves in the FET channel[62]. Log-periodic circular-toothed antennas at the source and gate electrodes were used to couple the 0.3-THz radiation of an electronic source. The measured dependence of the photovoltage, V_{ph}, on $(1/\sigma)(d\sigma/dV_G)$, with V_G the gate voltage, was shown to be in qualitative agreement with the prediction of a diffusive theoretical model[62], thereby proving that the detectors operate in the so-called broadband overdamped regime[58]. A maximum $R_v = 1.3$ V W^{-1} (or $R_{ph} = 1.3$ mA W^{-1} in photocurrent mode) and minimum NEP ~1 nW Hz$^{-0.5}$ were reported[63] (Fig. 6c), making the proposed technology exportable in a realistic setting to enable large-area, fast imaging of macroscopic samples (Fig. 6d). Further experiments at higher frequencies (3.11 THz) for back-gated antenna-coupled graphene FETs[119] showed photovoltage signals of a few microvolts.

Graphene-based broadband THz detectors working at room temperature were demonstrated[120] with R_v ~5 nA W^{-1} and fast response rise times (~50 ps) at 2.5 THz, which makes them already suitable for timing applications. The device in ref. 120 employed a log-periodic THz antenna[120] with a central interdigitated comb providing the electrical contact to the SLG. PTE graphene THz detectors, operating at 2.5 THz and based on exfoliated SLG with a pattern of asymmetric metal contacts, were also reported[121].

Photodetectors based on other 2D materials. The bulk properties of TMDs have been investigated for many decades[122], and the quest to produce 2D layers started with the pioneering work of Frindt and

Table 1 | Performance parameters.

Reference	Description	Responsivity	Detector type	Bandwidth	Wavelength	IQE (%)	EQE (%)
18,19	Graphene–metal junction	6.1 mA W^{-1}	Photocurrent (PV/PTE)	>40 GHz	Visible, NIR	10	0.5
30,37,52	Graphene p–n junction	10 mA W^{-1}	Photocurrent (PTE)		Visible	35	2.5
20–22	Graphene coupled to waveguide	0.13 A W^{-1}	Photocurrent (PV/PTE)	>20 GHz	1.3–2.75 μm	10	10
90	Graphene–silicon heterojunction	0.435 A W^{-1}	Schottky photodiode	1 kHz	0.2–1 μm		65
31	Biased graphene at room temperature	0.2 mA W^{-1}	Bolometric		Visible, infrared		
94	Dual-gated bilayer-graphene at low temperature	10^5 V W^{-1}	Bolometric	>1 GHz	10 μm		
105	Hybrid graphene–QD	10^8 A W^{-1}	Phototransistor	100 Hz	0.3–2 μm	50	25
63	Graphene with THz antenna	1.2 V W^{-1}	Overdamped plasma waves		1,000 μm		
120	Graphene interdigitated THz antenna	5 nA W^{-1}	Photovoltaic and photoinduced bolometric	20 GHz	2.5 THz		
147,148	Graphene–TMD–graphene heterostructure	0.1 A W^{-1}	Vertical photodiode		<650 nm		30
130	Biased MoS_2	880 A W^{-1}	Photoconductor	0.1 Hz	<700 nm		
143	Graphene double-layer heterostructure	>1 A W^{-1}	Phototransistor	1 Hz	0.5–3.2 μm		
7,8,134	WSe_2 p–n junction	16 mA W^{-1}	p–n photodiode		<750 nm	60	3
136	GaS nanosheet	19.1 A W^{-1}	Photoconductor	>10 Hz	0.25–0.5 μm		

Yoffe[123] in 1963. The structural and optical properties of single-layer MoS_2 (1L-MoS_2) have been investigated since the 1980s[124]. But it is only following the interest in graphene that the research into other 2D materials has been revived. In particular, it is now clear that they have great potential for applications in optoelectronics. The properties of TMDs depend on their thickness. For example, MoS_2 has a bulk indirect bandgap of 1.3 eV, which becomes a direct bandgap of 1.8 eV in 1L-MoS_2 (refs 125,126). This changes the optical properties, such as absorption spectrum and photoluminescence. A 1,000-fold enhancement of the luminescence quantum yield for 1L-MoS_2 compared with bulk MoS_2 was shown in ref. 125. Valley polarization controlled by optical pumping was also demonstrated[127] in 1L-MoS_2, and polarization was maintained for longer than 1 ns.

Compared with classical direct-bandgap semiconductors, TMDs can offer additional advantages in the context of optoelectronics because of their mechanical flexibility and easy processing. Most TMD-based photodetectors operate under bias[128–132], as a photodiode (Fig. 7a–c) or photoconductor (Fig. 7d–f). For example, photoconductive 1L-MoS_2 detectors were realized with high external photoresponsivity of 880 A W^{-1} (ref. 130; Fig. 7e,f), but with very long response time (~9 s), and GaTe detectors were reported[133] with $R_{ph} = 10^4$ A W^{-1} and response time of 6 ms. Moreover, the ability to tune the bandgap by varying the number of layers allowed the detection of light at different wavelengths[132]. The limitations of these devices — large dark current and frequency response slower than 1 Hz — were tackled by employing split-gate electrodes underneath a 1L-WSe_2 to realize a p–n photodiode[7,8,134]. Photodetectors based on a multitude of other layered materials, including MoS_2 ($R_{ph} = 0.57$ A W^{-1})[131], GaSe ($R_{ph} = 2.8$ A W^{-1})[135], GaS ($R_{ph} = 19$ A W^{-1})[136], In_2Se_3 ($R_{ph} = 3.95$ A W^{-1})[137], black phosphorus[138] and WS_2 ($R_{ph} = 22$ μA W^{-1})[139], have been reported. The strong PTE effect measured at metal–TMD junctions can also be useful for applications in thermopower generation[140].

TMDs are a good illustration of the wide range of optical properties offered by 2D crystals. A promising approach to combine these properties and create multifunctional, high-performance materials consists in assembling graphene with other 2D crystals in heterogeneous stacks and hybrid devices. By combining graphene with MoS_2, a novel type of hybrid device was demonstrated[141,142], in which visible light absorption and charge trapping is provided by the MoS_2 layer, with R_{ph} ~5×10^8 A W^{-1} at room temperature, with QE ≈ 32%. The speed was limited to ~1 Hz, owing to the trapping lifetime of ~1 s. A related device, consisting of a pair of stacked SLG separated by a thin tunnel barrier, showed strong photogating of the channel conductance and ultra-broadband (visible–MIR) response with $R_{ph} > 1$ A W^{-1} in the MIR[143]. Novel transistor concepts based on vertical transport between two graphene electrodes separated by hexagonal boron nitride[144], MoS_2 or WS_2 layers were reported[145,146] (Fig. 7a-c). The same hybrid devices have shown potential for photodetector applications with R_{ph} ~0.1 A W^{-1} and EQE ≈ 30%[147,148]. In these devices, graphene layers are employed as work-function tunable electrodes, whereas TMDs are utilized as photoactive material, displaying strong light–matter interactions and photon absorption. Electron–hole pairs are created in the TMD and separated between the two neighbouring graphene layers, thus taking advantage of the whole graphene–TMD junction to produce photocurrent.

Application fields, challenges and perspectives

We now discuss the performance of current state-of-the-art GRM photodetection platforms. Because graphene is distinctly different as a material system, it possesses advantages but also disadvantages, leaving us with challenges to be addressed to achieve competitiveness in various application fields. We show the GRM performance parameters in Table 1.

High-speed applications. High-speed photodetection superior to existing technologies is desirable for optical communications. The intrinsic bandwidth of graphene-based photodetectors was measured[74] to be 262 GHz. Owing to the broadband absorption of graphene, photoresponsivity for visible, NIR and SWIR was shown to be fairly constant (up to ~3 μm; ref. 149), with R_{ph} up to ~0.13 A W^{-1}, exploiting integration with waveguides[21,22,150] or enhancements by plasmonics[82]. In terms of bandwidth, graphene is thus capable of outperforming other technologies being investigated for optical communications, such as monolithically integrated Ge (refs 151,152). High-speed photodetectors have also been realized with III–V semiconductors (>300 GHz)[153], but these are difficult to integrate with Si optical and electronic technologies. An outstanding challenge for graphene-based photodetectors remains the increase of responsivity and effective detection area. Heterostructure stacks of 2D materials for vertical photocurrent extraction have large detection areas[147] and may therefore address the latter issue. An additional advantage over existing technologies is that graphene is a platform for high-speed light modulation and detection on the same chip. Although the individual elements have been realized, the integration of an all-optical link and the implementation of large-scale circuitry remains an outstanding challenge. The results in ref. 73 imply that the light-generated anisotropic distribution of carriers in momentum space can be observed in electrical measurements, despite their relaxation on ultrafast timescales. This may pave the way to graphene-based photodetectors that can detect incident light and its polarization on ultrafast timescales, overcoming the time constant that has thus far been speed-limiting.

Highly sensitive detection. High-sensitivity photodetection has become a major functionality for many applications, such as remote sensing, biomedical imaging, optical communications and gas sensing. For applications where transparency and flexibility are important, GRM-based photodiodes represent a promising alternative. For applications where detection of SWIR to MIR is required, Si is not a suitable absorber, and III–V semiconductors offer an alternative, but they are costly and difficult to integrate with Si read-out electronics. GRM-based photodiodes, photoconductors and hybrid phototransistors are particularly promising because they exhibit high photoconductive gain due to the high mobility of GRMs, do not require high voltages and can be monolithically integrated with existing Si-based multipixel focal-plane arrays[105,106,108,141]. By sensitizing the GRM, the sensitivity range can cover ultraviolet–visible[154,155], as well as SWIR[110] and MIR[156]. The outstanding challenge of this type of photoconductive detectors is the dark current, which can be addressed by the read-out circuitry (similar to bolometric systems). The projected NEP (~10^{-17} W) and D^* (7×10^{13} Jones)[105] are on par with existing technologies, such as InGaAs. Challenges include improvement in speed (currently up to 100 Hz; ref. 105), large-scale production and integration of multipixel arrays. Alternatively, p–n photodiode-based TMDs exhibit high sensitivity (see, for example, refs 7,8) and low dark current. Improvements of the sensitive area and large-scale production are issues to address.

Mid-infrared detection. The detection of MIR light is important for biosensing, security and thermal imaging. For this frequency range, graphene can offer an appealing advantage compared with other materials: its plasmons could be used to resonantly enhance absorption for a wavelength that is tunable with a gate, offering *in situ* tunable spectral selectivity. The major outstanding challenge for this wavelength range is the carrier extraction, for example, by using p–n junctions in lateral or vertical structures, or by employing bolometric detection. Graphene bolometers have shown excellent performance[94] at low temperature, with NEP ~33 fW $\text{Hz}^{-0.5}$, comparable to existing technologies. The main challenge remains the matching of the high graphene impedance (tens of kΩ) to that of free space (377 Ω) for efficient photon coupling.

Terahertz detection. Photodetection of FIR radiation is relevant for a variety of strategic applications, ranging from medical diagnostics to process control, homeland security, metrology and cultural heritage. Commercially available THz detectors are based on thermal sensing elements that are either very slow (10–400 Hz modulation and NEP ~10^{-10} W $\text{Hz}^{-0.5}$) or require deep cryogenic cooling (4 K for superconducting hot-electron bolometers), whereas those exploiting fast nonlinear electronics (Schottky diodes) or high-mobility transistors are usually limited to sub-THz frequencies[157]. Graphene THz detectors have already been demonstrated for the range 0.29–0.38 THz with a NEP ~10^{-9} W $\text{Hz}^{-0.5}$ (ref. 62), and at 2 THz with a NEP ~10^{-8} W $\text{Hz}^{-0.5}$ (ref. 121). The combination of scalability at higher frequencies, the prospects for integration with Si-platforms and the potential for implementing flexible devices makes graphene highly competitive for a future generation of THz detection systems.

In summary, photodetection platforms based on GRMs are being developed at a remarkable pace, with great promise for a wide variety of application fields. For many types of detector, performance parameters have already been demonstrated at levels that are superior or on a par with existing technologies. Challenges remain to demonstrate their full potential and to exploit the distinct advantages of 2D crystals. The prospects for commercialization will depend not just on the detector performance, but also on some of their distinct advantages and capabilities, in addition to the ability to realize production of large-scale, high-quality GRMs at a low cost, and to establish large-scale integration with existing photonic and electronic platforms, such as CMOS technologies.

Received 10 April 2014; accepted 27 August 2014;

References

1. Bonaccorso, F., Sun, Z., Hasan, T. & Ferrari, A. C. Graphene photonics and optoelectronics. *Nature Photon.* **4,** 611–622 (2010).
2. Ferrari, A. C. *et al.* Science and technology roadmap for graphene, related two-dimensional crystals, and hybrid systems. *Nanoscale* (in the press).
3. Sun, Z. *et al.* Graphene mode-locked ultrafast laser. *ACS Nano* **4,** 803–810 (2010).
4. Koppens, F. H. L., Chang, D. E. & García de Abajo, F. J. Graphene plasmonics: A platform for strong light–matter interactions. *Nano Lett.* **11,** 3370–3377 (2011).
5. Grigorenko, A. N., Polini, M. & Novoselov, K. S. Graphene plasmonics. *Nature Photon.* **6,** 749–758 (2012).
6. Kim, K. S. *et al.* Large-scale pattern growth of graphene films for stretchable transparent electrodes. *Nature* **457,** 706–710 (2009).
7. Pospischil, A., Furchi, M. M. & Mueller, T. Solar-energy conversion and light emission in an atomic monolayer p–n diode. *Nature Nanotech.* **9,** 257–261 (2014).
8. Baugher, B. W. H., Churchill, H. O. H., Yang, Y. & Jarillo-Herrero, P. Optoelectronic devices based on electrically tunable p–n diodes in a monolayer dichalcogenide. *Nature Nanotech.* **9,** 262–267 (2014).
9. Liu, M. *et al.* A graphene-based broadband optical modulator. *Nature* **474,** 64–67 (2011).
10. Low, T. & Avouris, P. Graphene plasmonics for terahertz to mid-infrared applications. *ACS Nano* **8,** 1086–1101 (2014).
11. Dawlaty, J. M., Shivaraman, S., Chandrashekhar, M., Rana, F. & Spencer, M. G. Measurement of ultrafast carrier dynamics in epitaxial graphene. *Appl. Phys. Lett.* **92,** 42116 (2008).
12. Brida, D. *et al.* Ultrafast collinear scattering and carrier multiplication in graphene. *Nature Commun.* **4,** 1987 (2013).
13. Dawlaty, J. M. *et al.* Measurement of the optical absorption spectra of epitaxial graphene from terahertz to visible. *Appl. Phys. Lett.* **93,** 131905 (2008).
14. Nair, R. R. *et al.* Fine structure constant defines visual transparency of graphene. *Science* **320,** 1308 (2008).
15. Kuzmenko, A. B., van Heumen, E., Carbone, F. & van der Marel, D. Universal optical conductance of graphite. *Phys. Rev. Lett.* **100,** 117401 (2008).
16. Li, Z. Q. *et al.* Dirac charge dynamics in graphene by infrared spectroscopy. *Nature Phys.* **4,** 532–535 (2008).
17. Wang, F. *et al.* Gate-variable optical transitions in graphene. *Science* **320,** 206–209 (2008).
18. Xia, F., Mueller, T., Lin, Y.-M., Valdes-Garcia, A. & Avouris, P. Ultrafast graphene photodetector. *Nature Nanotech.* **4,** 839–843 (2009).
19. Mueller, T., Xia, F. & Avouris, P. Graphene photodetectors for high-speed optical communications. *Nature Photon.* **4,** 297–301 (2010).
20. Gan, X. *et al.* Chip-integrated ultrafast graphene photodetector with high responsivity. *Nature Photon.* **7,** 883–887 (2013).
21. Pospischil, A. *et al.* CMOS-compatible graphene photodetector covering all optical communication bands. *Nature Photon.* **7,** 892–896 (2013).
22. Wang, X., Cheng, Z., Xu, K., Tsang, H. K. & Xu, J. High-responsivity graphene/silicon-heterostructure waveguide photodetectors. *Nature Photon.* **7,** 888–891 (2013).

23. Novoselov, K. S. & Castro Neto, A. H. Two-dimensional crystals-based heterostructures: materials with tailored properties. *Phys. Scripta* **T146,** 014006 (2012).
24. Bonaccorso, F. *et al.* Production and processing of graphene and 2D crystals. *Mater. Today* **15,** 564–589 (December, 2012).
25. Wilson, J. A. & Yoffe, A. D. The transition metal dichalcogenides discussion and interpretation of the observed optical, electrical and structural properties. *Adv. Phys.* **18,** 193–335 (1969).
26. Peters, E. C., Lee, E. J. H., Burghard, M. & Kern, K. Gate dependent photocurrents at a graphene p–n junction. *Appl. Phys. Lett.* **97,** 193102 (2010).
27. Rao, G., Freitag, M., Chiu, H.-Y., Sundaram, R. S. & Avouris, P. Raman and photocurrent imaging of electrical stress-induced p–n junctions in graphene. *ACS Nano* **5,** 5848–5854 (2011).
28. Mueller, T., Xia, F., Freitag, M., Tsang, J. & Avouris, P. Role of contacts in graphene transistors: A scanning photocurrent study. *Phys. Rev. B* **79,** 245430 (2009).
29. Farmer, D. B. *et al.* Chemical doping and electron-hole conduction asymmetry in graphene devices. *Nano Lett.* **9,** 388–392 (2009).
30. Lemme, M. C. *et al.* Gate-activated photoresponse in a graphene p-n junction. *Nano Lett.* **11,** 4134–4137 (2011).
31. Freitag, M., Low, T., Xia, F. & Avouris, P. Photoconductivity of biased graphene. *Nature Photon.* **7,** 53–59 (2012).
32. Kim, R., Perebeinos, V. & Avouris, P. Relaxation of optically excited carriers in graphene. *Phys. Rev. B* **84,** 075449 (2011).
33. Malic, E., Winzer, T., Bobkin, E. & Knorr, A. Microscopic theory of absorption and ultrafast many-particle kinetics in graphene. *Phys. Rev. B* **84,** 205406 (2011).
34. Tomadin, A., Brida, D., Cerullo, G., Ferrari, A. C. & Polini, M. Nonequilibrium dynamics of photoexcited electrons in graphene: Collinear scattering, Auger processes, and the impact of screening. *Phys. Rev. B* **88,** 035430 (2013).
35. Winzer, T., Knorr, A. & Malic, E. Carrier multiplication in graphene. *Nano Lett.* **10,** 4839–4843 (2010).
36. Xu, X., Gabor, N. M., Alden, J. S., van der Zande, A. M. & McEuen, P. L. Photo-thermoelectric effect at a graphene interface junction. *Nano Lett.* **10,** 562–566 (2010).
37. Gabor, N. M. *et al.* Hot carrier-assisted intrinsic photoresponse in graphene. *Science* **334,** 648–52 (2011).
38. Song, J. C. W., Rudner, M. S., Marcus, C. M. & Levitov, L. S. Hot carrier transport and photocurrent response in graphene. *Nano Lett.* **11,** 4688–4692 (2011).
39. Sun, D. *et al.* Ultrafast hot-carrier-dominated photocurrent in graphene. *Nature Nanotech.* **7,** 114–118 (2012).
40. Kotov, V. N., Uchoa, B., Pereira, V. M., Guinea, F. & Castro Neto, A. H. Electron–electron interactions in graphene: current status and perspectives. *Rev. Mod. Phys.* **84,** 1067–1125 (2012).
41. Tielrooij, K. J. *et al.* Photoexcitation cascade and multiple hot-carrier generation in graphene. *Nature Phys.* **9,** 248–252 (2013).
42. Song, J. C. W., Tielrooij, K. J., Koppens, F. H. L. & Levitov, L. S. Photoexcited carrier dynamics and impact-excitation cascade in graphene. *Phys. Rev. B* **87,** 155429 (2013).
43. Gierz, I. *et al.* Snapshots of non-equilibrium Dirac carrier distributions in graphene. *Nature Mater.* **12,** 1119–1124 (2013).
44. Johannsen, J. C. *et al.* Direct view of hot carrier dynamics in graphene. *Phys. Rev. Lett.* **111,** 027403 (2013).
45. Piscanec, S., Lazzeri, M., Mauri, F., Ferrari, A. C. & Robertson, J. Kohn anomalies and electron–phonon interactions in graphite. *Phys. Rev. Lett.* **93,** 185503 (2004).
46. Lazzeri, M., Piscanec, S., Mauri, F., Ferrari, A. & Robertson, J. Electron transport and hot phonons in carbon nanotubes. *Phys. Rev. Lett.* **95,** 236802 (2005).
47. Bistritzer, R. & MacDonald, A. H. Electronic cooling in graphene. *Phys. Rev Lett.* **102,** 206410 (2009).
48. Tse, W.-K. & Das Sarma, S. Energy relaxation of hot Dirac fermions in graphene. *Phys. Rev. B* **79,** 235406 (2009).
49. Song, J. C. W., Reizer, M. Y. & Levitov, L. S. Disorder-assisted electron–phonon scattering and cooling pathways in graphene. *Phys. Rev. Lett.* **109,** 106602 (2012).
50. Graham, M. W., Shi, S-F., Ralph, D. C., Park, J. & McEuen, P. L. Photocurrent measurements of supercollision cooling in graphene. *Nature Phys.* **9,** 103–108 (2012).
51. Betz, A. C. *et al.* Supercollision cooling in undoped graphene. *Nature Phys.* **9,** 109–112 (2012).
52. Freitag, M., Low, T. & Avouris, P. Increased responsivity of suspended graphene photodetectors. *Nano Lett.* **13,** 1644–1648 (2013).
53. Ashcroft, N. W. & Mermin, N. D. *Solid State Physics* 848 (Cengage Learning, 1976).
54. Castro Neto, A. H., Guinea, F., Peres, N. M. R., Novoselov, K. S. & Geim, A. K. The electronic properties of graphene. *Rev. Mod. Phys.* **81,** 109–162 (2009).
55. Soref, R. A. Silicon-based optoelectronics. *Proc. IEEE* **81,** 1687–1706 (1993).
56. Richards, P. L. Bolometers for infrared and millimeter waves. *J. Appl. Phys.* **76,** 1 (1994).
57. Rose, A. *Concepts in Photoconductivity and Allied Problems* (Krieger, 1978).
58. Dyakonov, M. & Shur, M. Shallow water analogy for a ballistic field effect transistor: New mechanism of plasma wave generation by dc current. *Phys. Rev. Lett.* **71,** 2465–2468 (1993).
59. Dyakonov, M. & Shur, M. Detection, mixing, and frequency multiplication of terahertz radiation by two-dimensional electronic fluid. *IEEE Trans. Electron Dev.* **43,** 380–387 (1996).
60. Giuliani, G. F. & Vignale, G. *Quantum Theory of the Electron Liquid* (Cambridge Univ. Press, 2005).
61. Tomadin, A. & Polini, M. Theory of the plasma-wave photoresponse of a gated graphene sheet. *Phys. Rev. B* **88,** 205426 (2013).
62. Vicarelli, L. *et al.* Graphene field-effect transistors as room-temperature terahertz detectors. *Nature Mater.* **11,** 865–871 (2012).
63. Spirito, D. *et al.* High performance bilayer-graphene terahertz detectors. *Appl. Phys. Lett.* **104,** 061111 (2014).
64. Park, J., Ahn, Y. H. & Ruiz-Vargas, C. Imaging of photocurrent generation and collection in single-layer graphene. *Nano Lett.* **9,** 1742–1746 (2009).
65. Lee, E. J. H., Balasubramanian, K., Weitz, R. T., Burghard, M. & Kern, K. Contact and edge effects in graphene devices. *Nature Nanotech.* **3,** 486–490 (2008).
66. Xia, F. *et al.* Photocurrent imaging and efficient photon detection in a graphene transistor. *Nano Lett.* **9,** 1039–1044 (2009).
67. Giovannetti, G. *et al.* Doping graphene with metal contacts. *Phys. Rev. Lett.* **101,** 26803 (2008).
68. Huard, B., Stander, N., Sulpizio, J. & Goldhaber-Gordon, D. Evidence of the role of contacts on the observed electron–hole asymmetry in graphene. *Phys. Rev. B* **78,** 121402 (2008).
69. Urich, A. *et al.* Silver nanoisland enhanced Raman interaction in graphene. *Appl. Phys. Lett.* **101,** 153113 (2012).
70. Withers, F., Bointon, T. H., Craciun, M. F. & Russo, S. All-graphene photodetectors. *ACS Nano* **7,** 5052–5057 (2013).
71. Prechtel, L. *et al.* Time-resolved ultrafast photocurrents and terahertz generation in freely suspended graphene. *Nature Commun.* **3,** 646 (2012).
72. Freitag, M., Low, T. & Avouris, P. Increased responsivity of suspended graphene photodetectors. *Nano Lett.* **13,** 1644–1648 (2013).
73. Echtermeyer, T. J. *et al.* Photothermoelectric and photoelectric contributions to light detection in metal–graphene–metal photodetectors. *Nano Lett.* **14,** 3733–3742 (2014).
74. Urich, A., Unterrainer, K. & Mueller, T. Intrinsic response time of graphene photodetectors. *Nano Lett.* **11,** 2804–2808 (2011).
75. Furchi, M. *et al.* Microcavity-integrated graphene photodetector. *Nano Lett.* **12,** 2773–2777 (2012).
76. Engel, M. *et al.* Light–matter interaction in a microcavity-controlled graphene transistor. *Nature Commun.* **3,** 906 (2012).
77. Shiue, R., Gan, X., Gao, Y., Li, L. & Yao, X. Enhanced photodetection in graphene-integrated photonic crystal cavity. *Appl. Phys. Lett.* **1,** 1–11 (2013).
78. Liu, J. *et al.* High-performance, tensile-strained Ge p–i–n photodetectors on a Si platform. *Appl. Phys. Lett.* **87,** 103501 (2005).
79. Su, S. *et al.* GeSn p–i–n photodetector for all telecommunication bands detection. *Opt. Express* **19,** 6400–6405 (2011).
80. Schedin, F. Surface-enhanced Raman spectroscopy of graphene. *ACS Nano* **4,** 5617–5626 (2010).
81. Mertens, J. *et al.* Controlling subnanometer gaps in plasmonic dimers using graphene. *Nano Lett.* **13,** 5033–5038 (2013).
82. Echtermeyer, T. J. *et al.* Strong plasmonic enhancement of photovoltage in graphene. *Nature Commun.* **2,** 458 (2011).
83. Liu, Y. *et al.* Plasmon resonance enhanced multicolour photodetection by graphene. *Nature Commun.* **2,** 579 (2011).
84. Jablan, M., Soljacic, M. & Buljan, H. Plasmons in graphene: Fundamental properties and potential applications. *Proc. IEEE* **101,** 1689–1704 (2013).
85. Thongrattanasiri, S., Koppens, F. H. L. & García de Abajo, F. J. Complete optical absorption in periodically patterned graphene. *Phys. Rev. Lett.* **108,** 047401 (2012).
86. Freitag, M. *et al.* Photocurrent in graphene harnessed by tunable intrinsic plasmons. *Nature Commun.* **4,** 1951 (2013).
87. Chen, C.-C., Aykol, M., Chang, C.-C., Levi, A. F. J. & Cronin, S. B. Graphene–silicon Schottky diodes. *Nano Lett.* **11,** 1863–1867 (2011).
88. Li, X. *et al.* Graphene-on-silicon Schottky junction solar cells. *Adv. Mater.* **22,** 2743–2748 (2010).
89. Miao, X. *et al.* High efficiency graphene solar cells by chemical doping. *Nano Lett.* **12,** 2745–2750 (2012).

90. An, X., Liu, F., Jung, Y. J. & Kar, S. Tunable graphene-silicon heterojunctions for ultrasensitive photodetection. *Nano Lett.* **13,** 909–916 (2013).
91. Tongay, S., Schumann, T. & Hebard, A. F. Graphite based Schottky diodes formed on Si, GaAs, and 4H-SiC substrates. *Appl. Phys. Lett.* **95,** 222103 (2009).
92. Tongay, S. *et al.* Rectification at graphene–semiconductor interfaces: Zero-gap semiconductor-based diodes. *Phys. Rev. X* **2,** 011002 (2012).
93. Amirmazlaghani, M., Raissi, F., Habibpour, O., Vukusic, J. & Stake, J. Graphene–Si Schottky IR detector. *IEEE J. Quantum Electron.* **49,** 589–594 (2013).
94. Yan, J. *et al.* Dual-gated bilayer graphene hot-electron bolometer. *Nature Nanotech.* **7,** 472–478 (2012).
95. Tan, Y.-W., Zhang, Y., Stormer, H. L. & Kim, P. Temperature dependent electron transport in graphene. *Eur. Phys. J. Spec. Top.* **148,** 15–18 (2007).
96. Oostinga, J. B., Heersche, H. B., Liu, X., Morpurgo, A. F. & Vandersypen, L. M. K. Gate-induced insulating state in bilayer graphene devices. *Nature Mater.* **7,** 151–157 (2008).
97. Xia, F., Farmer, D. B., Lin, Y-M. & Avouris, P. Graphene field-effect transistors with high on/off current ratio and large transport band gap at room temperature. *Nano Lett.* **10,** 715–718 (2010).
98. Viljas, J. K. & Heikkilä, T. T. Electron–phonon heat transfer in monolayer and bilayer graphene. *Phys. Rev. B* **81,** 245404 (2010).
99. Betz, A. C. *et al.* Hot electron cooling by acoustic phonons in graphene. *Phys. Rev. Lett.* **109,** 056805 (2012).
100. Han, Q. *et al.* Highly sensitive hot electron bolometer based on disordered graphene. *Sci. Rep.* **3,** 3533 (2013).
101. Vora, H., Kumaravadivel, P., Nielsen, B. & Du, X. Bolometric response in graphene based superconducting tunnel junctions. *Appl. Phys. Lett.* **100,** 153507 (2012).
102. Du, X., Prober, D. E., Vora, H. & Mckitterick, C. B. Graphene-based bolometers. *Graphene 2D Mater.* **1,** 1–22 (2014).
103. Ryzhii, V. The theory of quantum-dot infrared phototransistors. *Semicond. Sci. Technol.* **11,** 759–765 (1996).
104. Rowe, M. A. *et al.* Single-photon detection using a quantum dot optically gated field-effect transistor with high internal quantum efficiency. *Appl. Phys. Lett.* **89,** 253505 (2006).
105. Konstantatos, G. *et al.* Hybrid graphene–quantum dot phototransistors with ultrahigh gain. *Nature Nanotech.* **7,** 363–368 (2012).
106. Sun, Z. *et al.* Infrared photodetectors based on CVD-grown graphene and PbS quantum dots with ultrahigh responsivity. *Adv. Mater.* **24,** 5878–5883 (2012).
107. Klekachev, A. V. *et al.* Electron accumulation in graphene by interaction with optically excited quantum dots. *Physica E* **43,** 1046–1049 (2011).
108. Guo, W. *et al.* Oxygen-assisted charge transfer between ZnO quantum dots and graphene. *Small* **9,** 3031–3036 (2013).
109. McDonald, S. A. *et al.* Solution-processed PbS quantum dot infrared photodetectors and photovoltaics. *Nature Mater.* **4,** 138–142 (2005).
110. Konstantatos, G. *et al.* Ultrasensitive solution-cast quantum dot photodetectors. *Nature* **442,** 180–183 (2006).
111. Böberl, M., Kovalenko, M. V., Gamerith, S., List, E. J. W. & Heiss, W. Inkjet-printed nanocrystal photodetectors operating up to 3 μm wavelengths. *Adv. Mater.* **19,** 3574–3578 (2007).
112. Chen, S-Y. *et al.* Biologically inspired graphene-chlorophyll phototransistors with high gain. *Carbon* **63,** 23–29 (2013).
113. Fang, Z. *et al.* Plasmon-induced doping of graphene. *ACS Nano* **6,** 10222–10228 (2012).
114. Sizov, F. & Rogalski, A. THz detectors. *Prog. Quantum Electron.* **34,** 278–347 (2010).
115. Principi, A., Vignale, G., Carrega, M. & Polini, M. Impact of disorder on Dirac plasmon losses. *Phys. Rev. B* **88,** 121405 (2013).
116. Principi, A., Vignale, G., Carrega, M. & Polini, M. Intrinsic lifetime of Dirac plasmons in graphene. *Phys. Rev. B* **88,** 195405 (2013).
117. Ryzhii, V. & Ryzhii, M. Graphene bilayer field-effect phototransistor for terahertz and infrared detection. *Phys. Rev. B* **79,** 245311 (2009).
118. Ryzhii, V., Satou, A. & Otsuji, T. Plasma waves in two-dimensional electron–hole system in gated graphene heterostructures. *J. Appl. Phys.* **101,** 024509 (2007).
119. Knap, W. *et al.* Nanometer size field effect transistors for terahertz detectors. *Nanotechnology* **24,** 214002 (2013).
120. Mittendorff, M. *et al.* Ultrafast graphene-based broadband THz detector. *Appl. Phys. Lett.* **103,** 021113 (2013).
121. Cai, X. *et al.* Sensitive room-temperature terahertz detection via photothermoelectric effect in graphene. Preprint at http://arxiv.org/abs/1305.3297 (2013).
122. Fivaz, R., Mooser, E. & Moose, E. Mobility of charge carriers in semiconducting layer structures. *Phys. Rev.* **163,** 743–755 (1967).
123. Frindt, R. F. & Yoffe, A. D. Physical properties of layer structures: Optical properties and photoconductivity of thin crystals of molybdenum disulphide. *Proc. R. Soc. A* **273,** 69–83 (1963).
124. Joensen, P., Frindt, R. F. & Morrison, S. R. Single-layer MoS$_2$. *Mater. Res. Bull.* **21,** 457–461 (1986).
125. Mak, K. F., Lee, C., Hone, J., Shan, J. & Heinz, T. F. Atomically thin MoS$_2$: A new direct-gap semiconductor. *Phys. Rev. Lett.* **105,** 136805 (2010).
126. Splendiani, A. *et al.* Emerging photoluminescence in monolayer MoS$_2$. *Nano Lett.* **10,** 1271–1275 (2010).
127. Zeng, H., Dai, J., Yao, W., Xiao, D. & Cui, X. Valley polarization in MoS$_2$ monolayers by optical pumping. *Nature Nanotech.* **7,** 490–493 (2012).
128. Yin, Z. *et al.* Single-layer MoS$_2$ phototransistors. *ACS Nano* **6,** 74–80 (2012).
129. Choi, W. *et al.* High-detectivity multilayer MoS$_2$ phototransistors with spectral response from ultraviolet to infrared. *Adv. Mater.* **24,** 5832–5836 (2012).
130. Lopez-Sanchez, O., Lembke, D., Kayci, M., Radenovic, A. & Kis, A. Ultrasensitive photodetectors based on monolayer MoS$_2$. *Nature Nanotech.* **8,** 497–501 (2013).
131. Tsai, D.-S. *et al.* Few-layer MoS$_2$ with high broadband photogain and fast optical switching for use in harsh environments. *ACS Nano* **7,** 3905–3911 (2013).
132. Lee, H. S. *et al.* MoS$_2$ nanosheet phototransistors with thickness-modulated optical energy gap. *Nano Lett.* **12,** 3695–700 (2012).
133. Liu, F. *et al.* High-sensitivity photodetectors based on multilayer GaTe flakes. *ACS Nano* **8,** 752–760 (2014).
134. Ross, J. S. *et al.* Electrically tunable excitonic light-emitting diodes based on monolayer WSe$_2$ p–n junctions. *Nature Nanotech.* **9,** 268–272 (2014).
135. Hu, P., Wen, Z., Wang, L., Tan, P. & Xiao, K. Synthesis of few-layer GaSe nanosheets for high performance photodetectors. *ACS Nano* **6,** 5988–5994 (2012).
136. Hu, P. *et al.* Highly responsive ultrathin GaS nanosheet photodetectors on rigid and flexible substrates. *Nano Lett.* **13,** 1649–1654 (2013).
137. Jacobs-Gedrim, R. B. *et al.* Extraordinary photoresponse in two-dimensional In$_2$Se$_3$ nanosheets. *ACS Nano* **8,** 514–521 (2014).
138. Buscema, M. *et al.* Fast and broadband photoresponse of few-layer black phosphorus field-effect transistors. *Nano Lett.* **14,** 3347–3352 (2014).
139. Perea-López, N. *et al.* Photosensor device based on few-layered WS$_2$ films. *Adv. Funct. Mater.* **23,** 5511–5517 (2013).
140. Buscema, M. *et al.* Large and tunable photothermoelectric effect in single-layer MoS$_2$. *Nano Lett.* **13,** 358–363 (2013).
141. Roy, K. *et al.* Graphene–MoS$_2$ hybrid structures for multifunctional photoresponsive memory devices. *Nature Nanotech.* **8,** 826–830 (2013).
142. Zhang, W. *et al.* Ultrahigh-gain photodetectors based on atomically thin graphene–MoS$_2$ heterostructures. *Sci. Rep.* **4,** 3826 (2014).
143. Liu, C-H., Chang, Y., Norris, T. B. & Zhong, Z. Graphene photodetectors with ultra-broadband and high responsivity at room temperature. *Nature Nanotech.* **9,** 273–278 (2014).
144. Britnell, L. *et al.* Field-effect tunneling transistor based on vertical graphene heterostructures. *Science* **335,** 947–950 (2012).
145. Georgiou, T. *et al.* Vertical field-effect transistor based on graphene–WS$_2$ heterostructures for flexible and transparent electronics. *Nature Nanotech.* **8,** 100–103 (2013).
146. Bernardi, M., Palummo, M. & Grossman, J. C. Extraordinary sunlight absorption and one nanometer thick photovoltaics using two-dimensional monolayer materials. *Nano Lett.* **13,** 3664–3670 (2013).
147. Britnell, L. *et al.* Strong light-matter interactions in heterostructures of atomically thin films. *Science* **340,** 1311–1314 (2013).
148. Yu, W. J. *et al.* Highly efficient gate-tunable photocurrent generation in vertical heterostructures of layered materials. *Nature Nanotech.* **8,** 952–958 (2013).
149. Zhang, B. Y. *et al.* Broadband high photoresponse from pure monolayer graphene photodetector. *Nature Commun.* **4,** 1811 (2013).
150. Gan, X. *et al.* Strong enhancement of light–matter interaction in graphene coupled to a photonic crystal nanocavity. *Nano Lett.* **12,** 5626–5631 (2012).
151. Chen, L. & Lipson, M. Ultra-low capacitance and high speed germanium photodetectors on silicon. *Opt. Express* **17,** 7901–7906 (2009).
152. Novack, A. *et al.* Germanium photodetector with 60 GHz bandwidth using inductive gain peaking. *Opt. Express* **21,** 28387 (2013).
153. Ito, H., Furuta, T., Kodama, S., Watanabe, S. & Ishibashi, T. InP/lnGaAs uni-travelling-carrier photodiode with 220 GHz bandwidth. *Electron. Lett.* **35,** 1556–1557 (1999).
154. Sukhovatkin, V., Hinds, S., Brzozowski, L. & Sargent, E. H. Colloidal quantum-dot photodetectors exploiting multiexciton generation. *Science* **324,** 1542–1544 (2009).
155. Konstantatos, G., Clifford, J., Levina, L. & Sargent, E. H. Sensitive solution-processed visible-wavelength photodetectors. *Nature Photon.* **1,** 531–534 (2007).

156. Keuleyan, S., Lhuillier, E., Brajuskovic, V. & Guyot-Sionnest, P. Mid-infrared HgTe colloidal quantum dot photodetectors. *Nature Photon.* **5,** 489–493 (2011).
157. Tonouchi, M. Cutting-edge terahertz technology. *Nature Photon.* **1,** 97–105 (2007).

Acknowledgements

We acknowledge A. Tomadin, V. Pellegrini, A. Tredicucci, J. Song, K-J. Tielrooij, L. Levitov, P. Jarillo-Herrero, F. Bonaccorso, S. Kar, A. Kis, E. Lidorikis and T. J. Echtermeyer for useful discussions. We acknowledge funding from the EU Graphene Flagship (contract no. 604391), The Italian Ministry of Education, University, and Research (MIUR) through the program 'FIRB—Futuro in Ricerca 2010', Projects PLASMOGRAPH (Grant No. RBFR10M5BT) and FRONTIER (grant number RBFR10LULP), the Fundacicio Cellex Barcelona, the Career integration grant 294056 (GRANOP), ERC grants CarbonLight, Hetero2D, the Austrian Science Fund FWF (START Y-539), EU grants GENIUS, MEM4WIN, EPSRC Grants EP/K01711X/1, EP/K017144/1, EP/L016087/1 and a Royal Society Wolfson Research Merit Award.

Additional information

Reprints and permissions information is available online at http://www.nature.com/reprints. Correspondence and request for materials should be addressed to F.H.L.K.

Competing financial interests

The authors declare no competing financial interests.